Materials Advances

ROYAL SOCIETY OF CHEMISTRY

PAPER

View Article Online
View Journal | View Issue

Cite this: *Mater. Adv.*, 2025, **6**, 7479

High photo detectivity and responsivity under time-dependent laser-irradiation of $Cu_{40}Sb_{40}S_{20}$ thin films for photodetector application

Laxmikanta Mahapatra,[af] Prabhukrupa C. Kumar,[b] P. Pradhan,[c] D. Alagarasan,[d] C. Sripan[e] and R. Naik *[b]

The emerging ternary Cu–Sb–S materials, belonging to the I–V–VI semiconductor family, with p-type conductivity are considered alternative absorber materials due to their tunable band gap energy in the 0.5–2 eV range and large absorption coefficient. Herein, we report the laser irradiation-induced optical, structural, and surface wettability changes in $Cu_{40}Sb_{40}S_{20}$ thin films at different lasing times. As observed from XRD data, the reduction in crystallite size upon laser irradiation increased lattice strain and dislocation density. The elemental composition of the film was verified using EDS spectra and elemental mapping. The surface structure changed with laser treatment, as probed from FESEM images, making the film more porous. The hydrophobicity of a laser-irradiated film decreased with increased surface energy, as confirmed by contact angle data. Microstructural changes were observed in Raman spectra, and defect density decreased, as revealed by photoluminescence spectra. Such a reduction in structural defects resulted in an increase in the energy gap to 1.792 eV from 1.596 eV upon 60-minute laser irradiation. Transparency is also enhanced, thus decreasing the extinction coefficient and optical density with illumination. The decrease in refractive index thus reduced optical nonlinearity in terms of third-order nonlinear susceptibility and nonlinear refractive index. Increased photosensitivity increased detectivity of the 60 min laser-illuminated film to 4.81×10^7 Jones from 1.7×10^6 Jones of the unirradiated film, which is beneficial for photodetection in the UV region.

Received 17th May 2025,
Accepted 6th September 2025

DOI: 10.1039/d5ma00505a

rsc.li/materials-advances

1. Introduction

The optical, electrical, structural, and morphological properties of thin films are greatly affected by any type of surface modification in their internal arrangements. Many external energy treatments on such films modify their different properties and are used for various optoelectronic applications. The methods used for providing external stimuli to the films include swift heavy ion irradiation, proton irradiation, gamma ray irradiation, thermal annealing, and laser irradiation.[1–5] Films are subjected to various laser irradiations, including exposure to instant and localized energy. This brings nonequilibrium conditions in the electronic and thermodynamic states. The heat generated from the incident laser intensity could be localized in space and time. The intensity of laser light at different irradiation times enables good control over the manipulation of film properties.[6] Modification of the properties of materials by laser irradiation is a powerful technique nowadays.[7] The method has some unique advantages as compared to conventional thermal annealing, such as reduced thermal exposure of the sample, rapid local heating, flexible management, and low influence on substrate temperature.[8]

The laser annealing of the sample also resulted in crystalline phase formation within a very short time upon irradiation. Surface morphology and electrical behavior are changed by such a process.[9] For many practical applications of chalcogen-containing materials, the tuning of their properties by laser irradiation is now a subject of systematic research.[10] Properties such as optical absorption and large optical reflectivity result from the transformation of the amorphous phase to the crystalline phase by laser irradiation.[11] For quick light–matter interaction, laser irradiation is now a substitute for the conventional thermal annealing method. In the laser illumination process,

[a] *Department of Physics, ITER, Siksha 'O' Anusandhan (Deemed to be University), Bhubaneswar, 751030, India*
[b] *Department of Engineering and Material Physics, ICT-IOC, Bhubaneswar, 751013, India*
[c] *Faculty of Engineering and Technology (ECE), Sri University, Cuttack, 754006, India. E-mail: ramakanta.naik@gmail.com*
[d] *Department of Physics, Nitte Meenakshi Institute of Technology (NMIT), Nitte (Deemed to be University), Bengaluru, 560064, India*
[e] *Department of Physics, Dayananda Sagar Academy of Technology and Management, Udayapura, Bengaluru, 560082, India*
[f] *Department of Physics, Nayagarh Autonomous College, Nayagarh, 752069, India*

the area of interaction is very small compared to the total area of the sample. For this purpose, either pulsed laser or continuous laser irradiation is preferred. Hence, a very simple, low-cost solid-state laser is utilized for irradiation on a $Cu_{40}Sb_{40}S_{20}$ thin film.

The availability of lone pair electrons in chalcogen-containing compounds is highly susceptible to laser-irradiated changes. It facilitates the formation of localized states by the excited carriers generated from light–matter interactions.[12] There are different magnitudes of changes in the structural, morphological, surface wettability, and electrical properties found in different chalcogen-containing compounds. The laser irradiation process basically strikes the photon energy from the light source on the film surface. The incident energy is responsible for the change in electrical, structural, optical, and morphological properties of materials. Such a process has advantages in the selection of a localized, selective, and fast material for the crystallization of chalcogenides.[13]

The decrement in energy gap and increment in absorption power and refractive index in $Ga_{15}Se_{81}In_4$ and $Ga_{15}Se_{79}In_6$ films by laser treatment are suitable for photovoltaic devices.[14] The enhanced microstructural order by laser irradiation in $Sb_{10}S_{40}Se_{50}$ thin films over its as-deposited condition indicates that the laser-irradiated film is more microstructurally disordered than the as-prepared film due to the improved crystallinity by densification of films.[15] The large change in absorption coefficient in laser-irradiated $Se_{75}S_{25-x}Cd_x$ is suitable for optical disc applications.[16] The observed changes in $Ga_{15}Se_{77}Ag_8$ chalcogenide thin films are due to light–matter interactions through lone-pair electrons, resulting in a change in the band gap. By the increase in laser irradiation time scale, the activation energy is found to decrease with increased dc conductivity for such films.[17] The femtosecond laser treatment-induced enhanced photostability in Ge–S thin films is very useful for the manufacture of micro–nano nonlinear photonic devices. These substrates are capable of functioning at high pumping power.[18] The enhancement in electrical conductivity with reduced activation energy in $Se_{90-x}Hg_xS_{10}$ films was observed with increased lasing time. The laser treatment decreased the density of defect states after irradiation due to the easy movement of photo-generated carriers.[19] The surface structuring through laser treatment is a prominent method for precise and localized material synthesis. The microstructure fabrication by femtosecond pulses on As_2Se_3 and As_2S_3 films might be used for photonic devices like fiber lasers, waveguides, and photonic crystals.[20] The formation of diffraction gratings from As_2Se_3, As_2S_3, $GeSe_2$, GeS_2, and $GeSe_3$ films is possible by illumination through a 213 nm deep ultraviolet nanosecond pulsed laser.[21] The change in morphology and structure by laser irradiation on the Sb_2S_3 film led to improved electrical and optical properties with increased photoconductivity.[22]

The pulse duration of the excitation laser influences a number of effects on chalcogenides. Photobleaching and photodarkening are the two dominant phenomena observed in continuous wave illumination. This occurs through the homopolar to heteropolar bond conversion process.[23] Hence, the laser irradiation at different time frames brings insight into the kinetics of changes in the film behavior. The increased nonlinear absorption coefficient in quaternary $Ag_{10}In_{15}S_{15}Se_{60}$ films decreases the nonlinear susceptibility and nonlinear refractive index.[24] The 532 nm laser heating in the $Sb_{10}S_{15}$-$In_{15}Se_{60}$ film at different time scales decreased the energy gap from 1.73 eV to 1.27 eV. The photodarkening phenomenon results in an enhanced refractive index, leading to an increased third-order nonlinear susceptibility and nonlinear refractive index that are suitable for different photonics devices.[25] The illumination effect under different lasing times in $Bi_{15}In_{20}Se_{65}$ thin films leads to decreased E_g and enhanced nonlinearity. It enables the improvement in two-photon absorption, making it suitable for photonic devices.[26] The $Ag_{10}Te_{10}As_{20}Se_{60}$ film under laser treatment at different time frames by a 532 nm continuous laser showed an increase in transparency in the IR region, leading to an increased energy gap from 1.73 eV to 2.01 eV after a 90-min irradiation. The resulting changes in different physical quantities make them suitable candidates for optoelectronic applications.[27] The intermixing of Ag_2S and As_2Se_3 layers from the Ag_2S/As_2Se_3 heterostructure results in the Ag–S–Se–As solid solution under laser irradiation at different time frames. There is a decrease in electrical susceptibility with enhanced optical conductivity and laser irradiation time duration.[28] Thus, by looking at the tuning in different parameters of the thin films at different lasing times, the present study relies on the time-dependent laser irradiation on $Cu_{40}Sb_{40}S_{20}$ thin films. The prime objective of the investigation is to observe the structural changes in terms of crystallinity, morphological modifications at the surface structure, changes in surface wettability properties, and various linear and nonlinear changes by laser irradiation at various time scales. The important aspect of this study is to observe the large change in photodetectivity and photoresponsivity upon laser irradiation for possible photodetector applications.

2. Experimental details

2.1. Thin film deposition and laser irradiation

The required bulk material for preparing the thin film was synthesized from the melt-quenching process. The appropriate amount of Cu, S, and Sb purchased from Sigma Aldrich with 99.999% purity was weighed and placed inside the ampoule at the required vacuum. The closed tube was kept in the furnace at 1100 °C for 24 h. For better mixing of the elements, the tube containing the ampoule inside the furnace was rotated continuously. The melt of the three elements was then quenched by liquid nitrogen very quickly by transferring the ampoule to LN_2. The ampoule was broken to collect the bulk sample, which was ground to make the powder form. The obtained powder sample was placed on a molybdenum boat inside the thermal coating unit chamber (Smart Coat, 3, HHV) 10^{-5} Torr (high vacuum). The voltage was increased slowly to start the deposition process, and the vapors from the melt of the powder sample were coated on the precleaned glass substrate attached

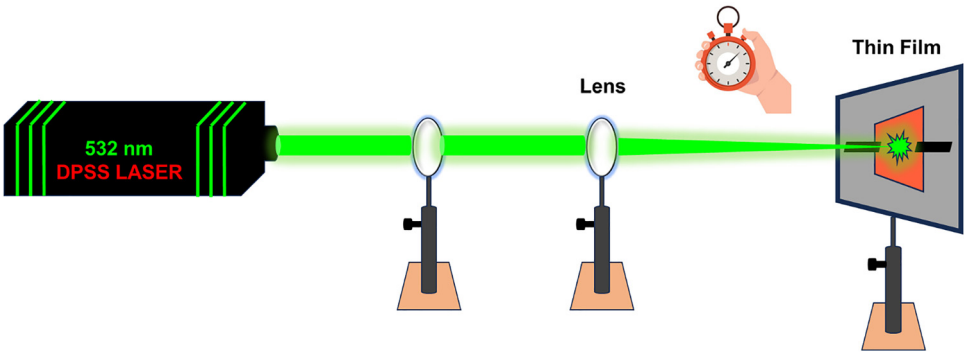

Scheme 1 Laser irradiation setup.

to the substrate holder inside the chamber. The slow motion of the motor of the substrate holder ensures the film deposition is uniform and smooth. The rate of deposition was very low, ~5 Å s^{-1}. The thickness controller attached to the instrument regulates the deposited thickness, and the deposited film is ~800 nm thick.

In order to study the laser treatment modifications in the deposited $Cu_{40}Sb_{40}S_{20}$ thin films, the pristine film was cut into several pieces and marked accordingly. The 532 nm DPSS laser source (Model: PSU-III-LED, C192055) of energy 2.33 eV with an intensity of 58 mW cm^{-2} was used to illuminate the cut film pieces at different time scales, such as 5, 10, 30, and 60 minutes. The irradiation process, which was done in dark conditions, is shown in Scheme 1, and the illuminated spot was 0.5 × 0.5 cm^2 in size. The temperature at the laser incident spot was calculated to be ~8–10 K (negligible) as per the procedure.[29,30] Such small heat is not enough to create any thermal change on the film surface. The observed changes are solely due to photon energy.

2.2. Characterization techniques

Various experimental techniques were adopted to extract the different properties and changes in the irradiated films compared to the as-deposited condition. The film thickness was cross-verified by a cross-sectional field emission scanning electron microscope (FESEM). The images were captured at high vacuum conditions with an operating voltage of 1–15 kV. The surface morphology images of the film were captured at different magnifications and in various positions. The elemental mapping, along with the constituent elements in the films, was obtained using energy-dispersive X-ray spectroscopy (EDS). The structure of the studied film was probed through X-ray diffraction (XRD) using a D8 Advance Bruker diffractometer. The 2θ angle scan on the films was done from 10–90° with a scan rate of 0.05° s^{-1}. The glancing angle for this purpose was 1°. The X-ray source is CuKα (λ = 0.1541 nm). The microstructural changes were probed through Raman and PL spectra. The data acquisition was carried out through a Renishaw (RE 04) microscope. The light excitation was done using a 532 nm laser, and the spectral resolution of the instrument was 0.5 nm. The core-level XPS spectra of the 60-minute laser-irradiated film were obtained using an Axis Ultra instrument (Kratos Analytical, UK) with an Al Kα X-ray source (1486.6 eV) under a vacuum of 2 × 10^{-9} Torr. The data was obtained in the backscattering mode through the CCD camera. The pendant drop method was used to measure surface wettability at room temperature through the DMe-211 Plus contact angle meter. The 1 μL-sized water droplet was

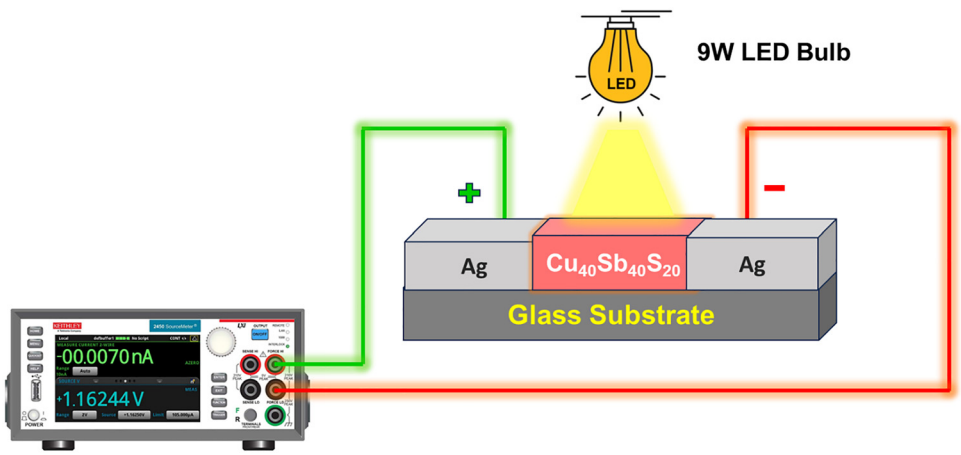

Scheme 2 Photodetection study through the Keithley 2450 source meter.

placed on the film, and the software measured the corresponding angle between the tangent to the liquid–vapor interface and the solid surfaces. The data was taken at 3–4 places to avoid any errors. The optical data was measured by a UV-visible spectrophotometer (JASCO V-770) from 500–2500 nm range. The different optical parameters were determined through appropriate relations.

The photoresponse of the studied films was recorded using a 2450 Keithley source meter with a 9 W LED bulb. The *IV* data were recorded from −10 V to +10 V with 0.05 V increments. The IV data were recorded in both dark and light conditions from a sample size of 5 × 5 mm^2. The schematic of the *IV* measurement is illustrated in Scheme 2.

3. Results and discussion

3.1. Morphology study by FESEM and EDX

Fig. 1(a) shows the cross-sectional image of the as-deposited $Cu_{40}Sb_{40}S_{20}$ thin film, which shows a thickness of ∼810 nm (∼800 nm as observed from the thickness controller). However, after 60 minutes of laser irradiation, the film thickness was found to be ∼820 nm (Fig. 1(b)). The small increase might be due to laser-induced expansion in the film by prolonged laser excitation. The image clearly demonstrates that the laser annealing of the film changes the surface morphology, as there is a clear change in the structure of the film.

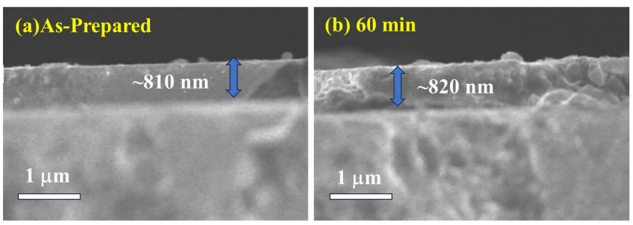

Fig. 1 Cross-sectional FESEM images of (a) the un-irradiated and (b) 60-minute laser illuminated films.

The FESEM images of the film surface of all the 60-minute irradiated films, along with the as-deposited one, are presented in Fig. 2 at different magnification scale bars. The as-deposited $Cu_{40}Sb_{40}S_{20}$ film surface structure looks smooth at a 1 μm scale (Fig. 2(a)), but clear crystallite morphology can be seen at the 100 nm scale (Fig. 2(b)). However, after a prolonged laser irradiation of 1 hour, the surface morphology clearly infers the change as pores can be clearly visualized in Fig. 2(i). The 100 nm scale image in Fig. 2(j) shows the magnified pores that were developed from laser irradiation. Such changes in the film morphology affect the porosity of the film and surface wettability, which will be discussed later. The FESEM images of all other films at two different magnifications are shown in Fig. 2(c–h). The 532 nm laser irradiation provides localized photon energy, which can lead to bond rearrangements within the film. The breaking of weaker homopolar bonds and subsequent reformation into heteropolar bonds introduces a slight lattice expansion, reflected as an increase in thickness. The FESEM surface images (Fig. 2) clearly show that prolonged irradiation induces pore formation, increasing the surface roughness and modifying the microstructure. Such morphological changes can also contribute to an apparent increase in film thickness in cross-sectional imaging. Thus, the reported increase in film thickness after 60 minutes of irradiation is consistent with laser-induced microstructural reorganization, bond rearrangement, and morphological expansion.

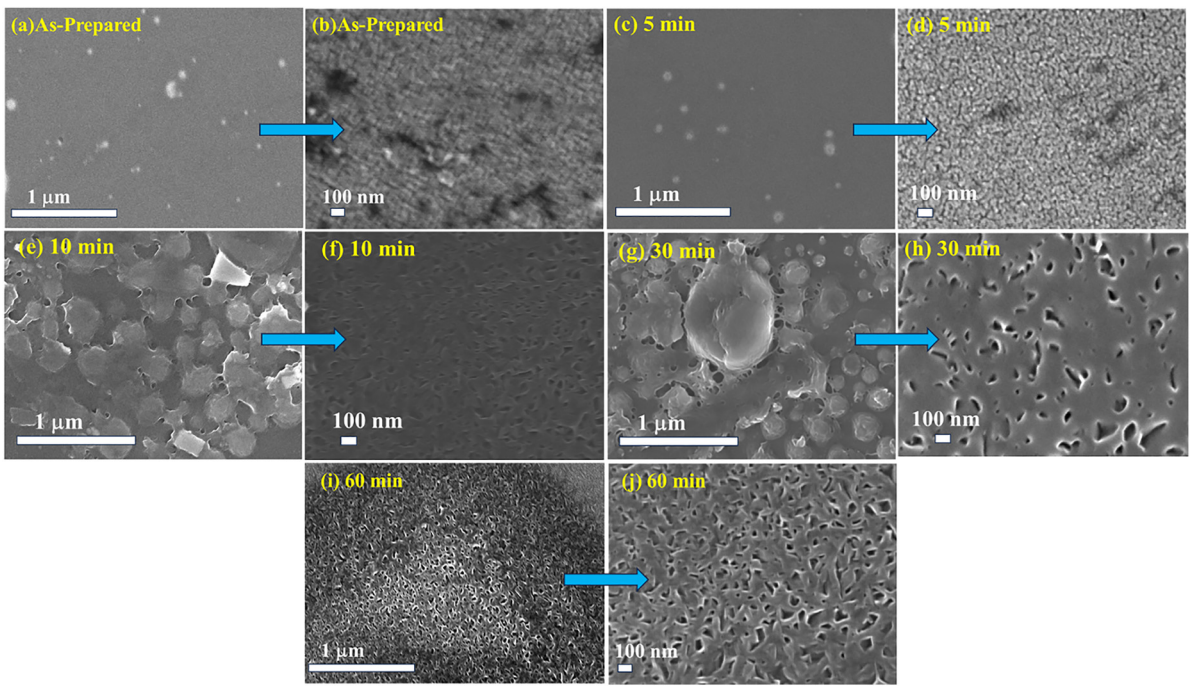

Fig. 2 FESEM pictures of (a and b) the as-prepared, (c and d) 5-min, (e and f) 10-min, (g and h) 30-min, and (i and j) 60-minute laser irradiated films.

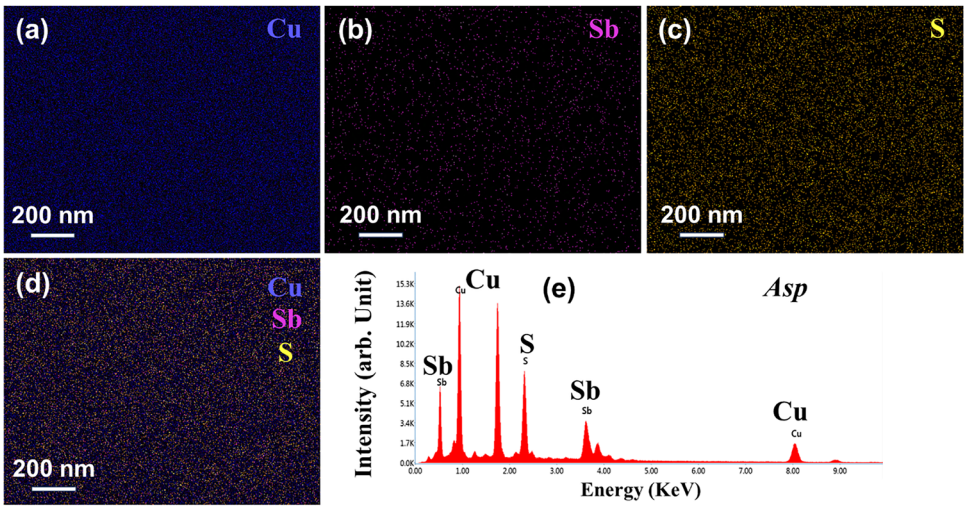

Fig. 3 Elemental mapping of individual elements (a) Cu, (b) Sb, and (c) S; (d) combined mapping; and (e) EDX spectra of the as-deposited film.

The confirmation regarding the presence of elements and the film composition was determined from the EDX data, as shown in Fig. 3. The elemental mapping showing the distribution of Cu, Sb, and S in the as-deposited film individually and combined is shown in Fig. 3. The EDX spectra show elemental peaks at their respective energy values. The EDX spectra of other films are presented in Fig. S1. The unassigned peaks are for the C and Au peaks, as they were used for charge correction. The elemental mapping of elements for the 60-minute laser-irradiated film is shown in Fig. S2.

3.2. Surface wettability study

The interaction of the film surface with liquids is probed by contact angle measurements, which indicate the nature of the film surface. If the film surface repels the water molecules, then it is called hydrophobic (water repelling), and the contact angle (θ_c) is generally greater than 90°. However, if the film surface attracts the water droplets, then the film possesses a hydrophilic nature (water-loving). In this case, the contact angle value is generally below 90°. For the low specific energy surface, the attraction of water is not strong enough, so the contact angle will be higher. Hence, a low surface energy surface becomes hydrophobic.[31] The contact angle measurement was performed on various laser-irradiated films, showing the hydrophobic nature illustrated in Fig. 4. It was noticed that the contact angle value slightly decreased upon laser irradiation on the film surface. The as-deposited film θ_c is 100.6°, which became 96.3° for the 60 min laser annealed film.

Such a decrease in the θ_c value upon laser irradiation is attributed to surface modification. The surface energy was calculated using Young's equation, $\gamma_{se} = \frac{\gamma_w(1+\cos\theta_c)^2}{4}$, where γ_w is the water surface tension (71.99 Nm m^{-1}),[32] and is presented in Table 1. The surface energy is found to increase with annealing, as shown in Table 1. The work of adhesion (W_{sl}), which presents the degree of binding strength between the film surface and water drop, is calculated by[33] $W_{sl} = \gamma_w(1 + \cos\theta_c)$. The W_{sl} value increased with annealing, along with the increase in surface energy. The hydrophobic nature of the films is very useful for self-cleaning activities.[34,35]

3.3. Structural study by XRD, Raman, and XPS

Fig. 5a shows the XRD pattern of the $Cu_{40}Sb_{40}S_{20}$ thin film. The distinct XRD peak at a glancing angle of 44.67° corresponds to

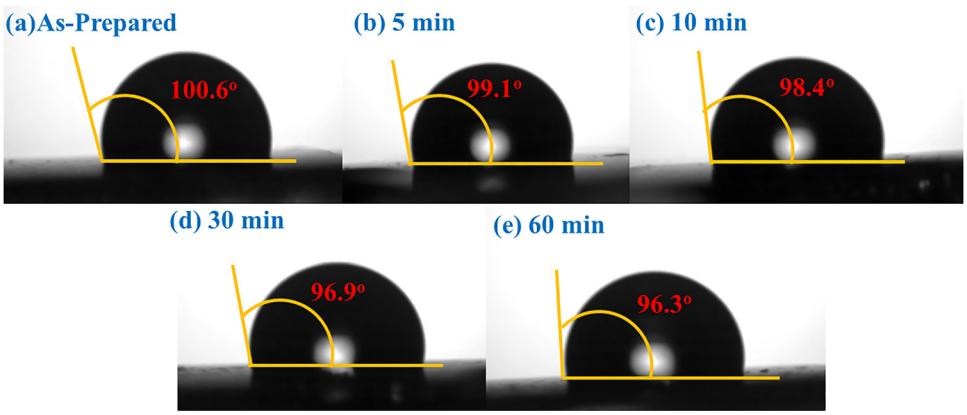

Fig. 4 Contact angle images of the laser-irradiated films at different time scales.

Table 1 Estimated parameters from contact angles of the films

Parameters/film	As-prepared	100 °C	150 °C	200 °C	250 °C
θ_C (degree)	100.6	99.1	98.4	96.9	96.3
γ_{se} (mN m^{-1})	11.98	12.75	13.12	13.93	14.26
W_{sl} (mN m^{-1})	58.74	60.71	61.47	63.34	64.09

the (220) crystallographic plane of the Cu_2S cubic phase. This matches well with the ICSD file number 00-012-0175. The other two minor peaks at around 64.69° and 82.10° are due to the crystallographic planes (640) and (752). These planes correspond to the cubic phase of $Cu_{12}Sb_4S_{13}$. This matches well with the ICSD reference file number 01-088-0282. The full-width at half maximum (FWHM) for the (220), (640), and (752) reflections was taken into consideration when estimating the crystallite size (D), micro-strain (ε), the number of crystallites per unit surface area (N_c), and dislocation density (δ).[36] The evaluated parameters are listed in Table 2. The 'D' value of the as-prepared sample is 21.66 nm. After treatment with LASER, the crystallite size decreased. The distribution and concentrations of crystal defects, such as dislocations, vacancies, twin faults, stacking faults, and lattice distortions, are brought on by mechanical stresses. In many instances, techniques other than diffraction cannot readily and statistically guarantee that such information is available.[37] The interference of various crystal lattices is the sole factor we need to take into account. This is because Bragg's law only applies to an ideal crystal or a crystal structure with an infinite lattice that repeats. Actual measurements of the crystal do not exhibit this characteristic. Scherrer initially derived the Scherrer equation, which is the relationship between the crystal grain size and the FWHM of the diffraction peak, as given below.[38]

$$\text{Crystallite size}\,(D) = \frac{k\lambda}{\beta\cos(\theta)} \quad (1)$$

Here, 'k' = 0.9 (Scherer constant), λ = 1.54 Å (X-ray wavelength). β is FWHM. θ is the glancing angle. The number of dislocation lines per unit volume of the crystal is given by[39]

Table 2 Structural parameters obtained from XRD data

Laser irradiation time	Average crystallite size (D) (nm)	Dislocation density (δ) × 10^{-3} (nm^{-2})	Micro-strain (ε) × 10^{-3}	N_c × 10^{-2} (nm^{-2})
Asp	21.66	2.131	91.94	24.97
5	19.97	2.507	110.04	30.13
10	19.52	2.624	127.77	15.44
30	18.58	2.896	140.51	26.61
60	16.49	3.677	225.57	14.22

$$\text{Dislocation density}\,(\delta) = \frac{1}{D^2} \quad (2)$$

The lattice strain is the deformation of the regular geometrical arrangement of atoms in a crystalline sample.[40]

$$\text{Lattice strain}\,(\varepsilon) = \frac{\beta}{4\tan(\theta)} \quad (3)$$

$$\text{Number of crystallites per unit surface area}\,(N_c) = \frac{d}{D^3} \quad (4)$$

Here, d = 810 nm, which is the thickness of the film.

Raman spectroscopy is generally a complementary method to obtain information regarding the phases associated with microstructural changes within the sample. The Raman spectra of unirradiated and illuminated samples are presented in Fig. 5(b). They show different peaks associated with the vibrational modes. It shows an intense peak at 353 cm^{-1} along with minor humps at 116, 146, 252, and 321 cm^{-1}. The main peak at 353 cm^{-1} is assigned to the cubic tetrahedrite Cu–Sb–S.[41] The decrease in peak intensity is observed with irradiation time scale, showing the decrease in defect state density. The peak observed at 321 cm^{-1} refers to the symmetric bending mode of the cubic tetrahedrite.[42] The Raman shifts at 252 cm^{-1} originated from Sb_2S_3, whereas the low-intensity peaks at 116 and 146 cm^{-1} are also due to the $CuSbS_2$ phase, as reported in the literature.[43,44]

XPS was employed to confirm the chemical composition and bonding states of the constituent elements in the deposited $Cu_{40}Sb_{40}S_{20}$ thin films. The survey scans of individual core

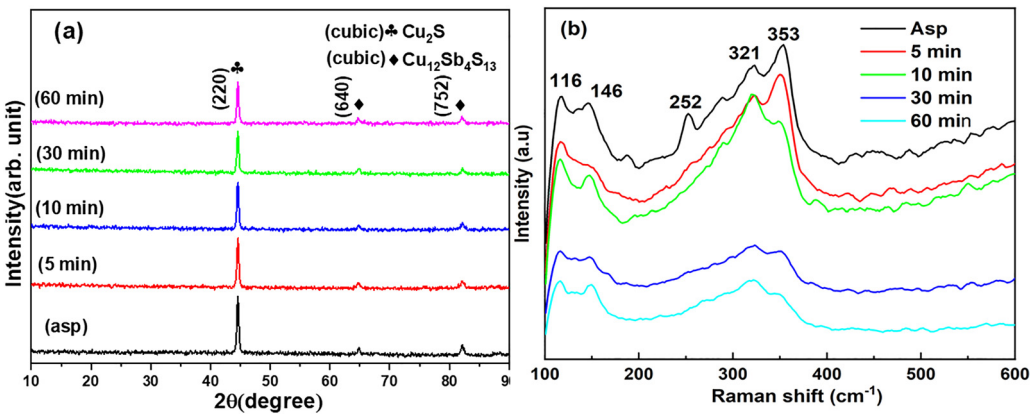

Fig. 5 (a) XRD pattern and (b) Raman spectra of the thin films at different irradiation time scales.

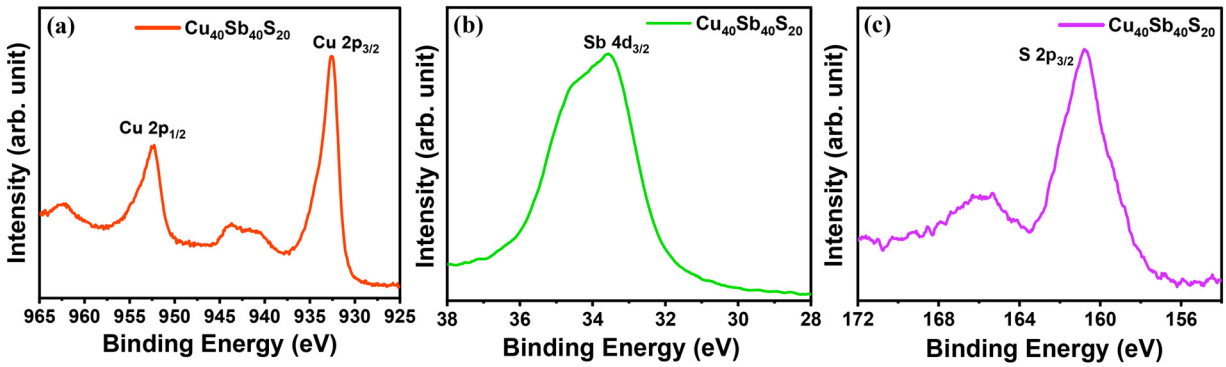

Fig. 6 Core level XPS spectra of constituent elements of the $Cu_{40}Sb_{40}S_{20}$ thin film: (a) Cu, (b) Sb, and (c) S.

levels shown in Fig. 6 clearly reveal the presence of Cu, Sb, and S, consistent with the target stoichiometry. The Cu 2p region (Fig. 6(a)) shows two main peaks at ~932.6 eV (Cu $2p_{3/2}$) and ~952.5 eV (Cu $2p_{1/2}$). The separation of 19.9 eV between these two peak positions indicates a +1 oxidation state of Cu, typically observed in copper sulfide systems.[36] The absence of strong satellite features indicates that Cu is predominantly in a stable sulfide environment. The Sb 4d region displayed in Fig. 6(b) demonstrates a distinct Sb $4d_{3/2}$ peak that appeared at ~33.8 eV, which is characteristic of Sb^{3+} in sulfide compounds, confirming the chemical bonding of antimony with sulfur.[45] Fig. 6(c) shows the S $2p_{3/2}$ peak centered around ~161.5 eV, which corresponds to S^{2-} in metal sulfides, providing direct evidence that sulfur is chemically incorporated into the thin film rather than segregating to the surface. Overall, the XPS analysis validates the successful incorporation of Cu, Sb, and S into the thin film in their expected chemical states, thereby confirming the formation of a sulfide-based compound. These results support the compositional claims made from EDX analysis and further rule out significant sulfur loss or surface migration during film deposition. Together with the EDX results, these findings validate the successful chemical incorporation and stoichiometric distribution of all constituent elements within the thin film.

3.4. Optical study by UV-visible and PL

Optical transmission of the studied films towards the electromagnetic radiation is shown in Fig. 7(a). It is evident that there

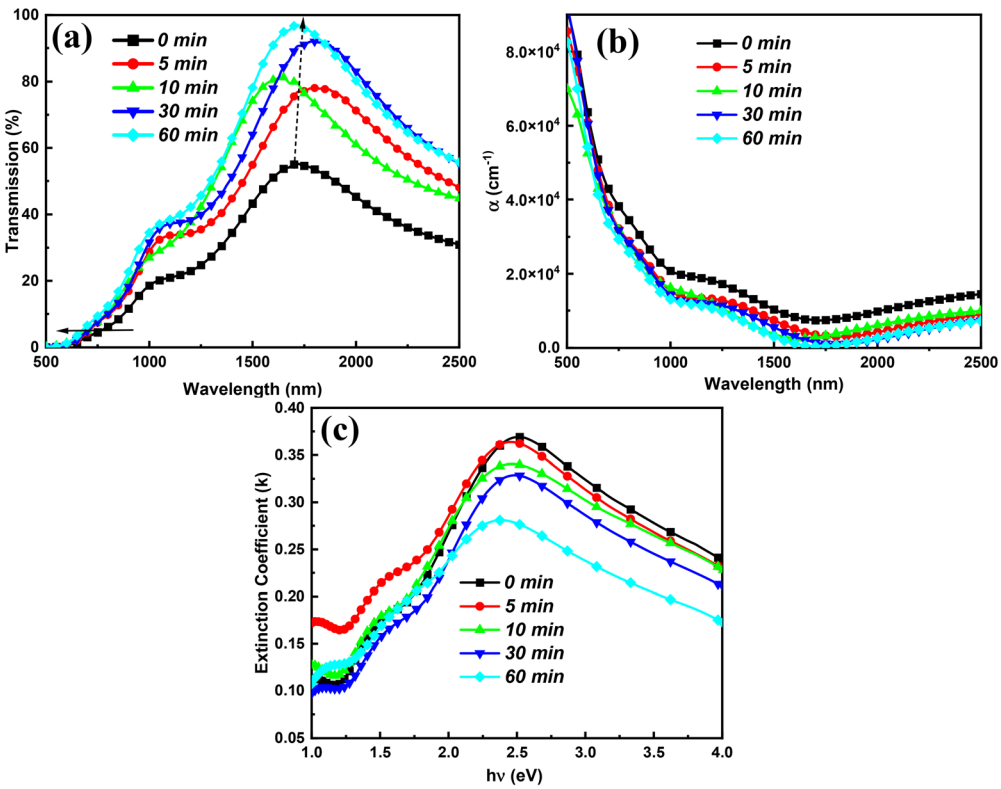

Fig. 7 (a) Transmission%, (b) absorption coefficient, and (c) extinction coefficient of the films.

is a gradual increase in transmission with laser irradiation time. The unirradiated film has ~55% transmission power, which gradually increased to ~97% for the 60-min laser-irradiated film. Such an increase in transmission upon laser irradiation is because of decreased defect states/scattering centers, which makes the film more transparent. Such a type of observation is also found for the other films with laser irradiation.[28,46] An absorption edge shift to a low wavelength regime also indicates an optical bandgap increase. In order to calculate the absorption strength, it is essential to determine the absorption coefficient (α), which is determined from the transmittance value with the relation,[28]

$$\text{Absorption coefficient } (\alpha) = \frac{1}{d}\left(\ln\frac{1}{T}\right) \quad (5)$$

Here, d = 810 nm (film thickness), and T is the transmittance.

The observed decrease in the 'α' value is evident from Fig. 7(b). Such a decrement with laser irradiation time scale is for the bond rearrangement mechanism with photon energy. Homopolar or wrong bonds generally break down with incident energy, and heteropolar bond creation occurs at the cost of such bonds.[40] The decrease in defect states resulted in a decrease in the absorption capability of the samples.

The loss in absorption is also depicted from another physical parameter, the so-called extinction coefficient (k). It is evaluated from the relation $k = \alpha\lambda/4\pi$. This quantity measures light loss occurring from scattering and absorption per unit distance of the medium. From Fig. 7(c), it is noticed that the k value decreased with irradiation time, supporting the decrease in absorption capability.

The optical density (OD) is also related to the absorption measurement of film thickness. It is associated with the film concentration at different thicknesses and the surface morphology of the samples. The value of OD is the product of 'α' and 'd' (OD = $\alpha \times d$). The OD value is less for the laser-irradiated film, as seen in Fig. 8(a). It is almost saturated at the higher energy side (lower wavelength), which implies the saturation of absorption capability after a certain length scale inside the film.

The most important optical parameter that infers the transition probability of the electrons from the valence to the conduction band is the bandgap (E_g). It is generally evaluated from the dependency of the absorption coefficient on incident energy ($h\nu$) within the strong absorption regime. The Tauc relation is used to determine the value of E_g through the relation,[47]

$$\alpha h\nu = B(E_g - h\nu)^s \quad (6)$$

Here, the different types of transitions are inferred from the value of the exponent factors. It carries different values for different types of optical transitions. For allowed optical transitions, s is equal to $\frac{1}{2}$ and 2 for direct and indirect transitions. The s value of 3/2 and 3 is for direct and indirect forbidden transitions.[48,49] For the present case, the transition is found to be a direct allowed one with s = 1/2. The band gap was

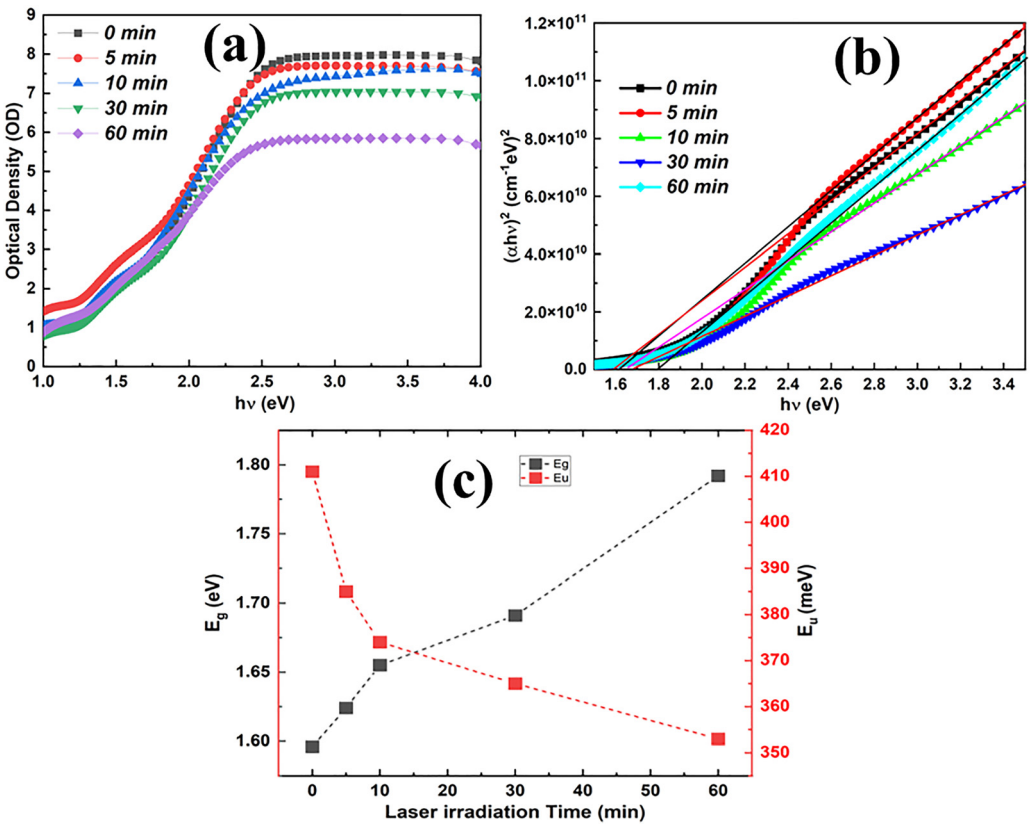

Fig. 8 (a) Optical density, (b) bandgap, and (c) variation of E_g and E_u of the films.

calculated from the *x*-intercept of the linear plot between $(\alpha h\nu)^2$ *vs.* $h\nu$ as shown in Fig. 8(b). The individual bandgap calculation plots for all the films are shown in Fig. S3. The direct optical bandgap is found to increase from 1.596 eV (un-irradiated) to 1.792 eV for the 60-minute laser-irradiated film. The E_g values are close to the bulk band gap of the Al–Sb alloy overlayers.[50] This increased value of the band gap is due to decreased surface dangling bonds, caused by particle agglomeration due to laser irradiation. Hence, the defects are reduced, and the lattice is undisrupted in highly polycrystalline films. Thus, because of laser irradiation, the localized state concentration in the band structure steadily decreased. The localised state change is for the decrease in the number of dangling bonds and defects. Consequently, the energy width of the localized states shrank, increasing the optical energy gap.[46,51] The increase in E_g value is associated with the increased value of B^2 (Tauc parameter). It is inversely related to the disorders, which can be found in the slope of the linear fitting of eqn (6). The obtained values, as given in Table 3, infer the increased value of B^2, depicting the decreased nature of the disorder and increased crystallinity that decreased the localized states and ultimately increased the gap value.

The other important parameter measuring the disorder strength is the Urbach energy measured from the region of $\alpha < 10^4$ cm^{-1}. It established an exponential relation with the absorption coefficient through the Urbach equation,[52]

$$\alpha = \alpha_0 \exp\left(\frac{h\nu}{E_U}\right) \quad (7)$$

α_0 is a constant, referring to the value at the bandgap point, and E_U is the Urbach energy. It measures the width of the tails of the localized states in the gap regime.[53,54] Consequently, both the α_0 and E_U values for films are calculated by plotting $(\ln \alpha)$ as a function of $h\nu$ and are listed in Table 3. The E_u value decreased with increased laser irradiation time, thus inferring a decrease in the width of the localized states and disorder value. This decrement in the width of the localized state leads to broadening of the absorption band, and hence the increase in the band gap. The change in E_u with E_g at different irradiation times is presented in Fig. 8(c). The primary cause of this is exciton–phonon interaction or electron–phonon interaction,[55] which can be expressed as the electron–phonon interaction strength (S_{e-p}). This parameter characterizes the expansion and growth of lattice constants. The lattice dimensions increase when this parameter increases, and *vice versa*. The electron–phonon interaction strength depends on the steepness parameter (σ), which defines the stiffness and sharpness of the absorption edge. The value of σ and S_{e-p} were calculated using the following equations,[56,57]

$$\sigma = \frac{k_B T}{E_U}, \quad S_{e-p} = \frac{2}{3\sigma} \quad (8)$$

Here, k_B is the Boltzmann's constant and T is the absolute temperature. The increased σ value corresponds to a decrease of S_{e-p}, as shown in Table 3. The decreased value of S_{e-p} leads to a decrease in lattice dimension through an increase in the energy gap. The change in the value of σ and S_{e-p} at different irradiation time scales is presented in Fig. 9(a).

Light dispersion in different propagation media is determined through the refractive index (n). It has both the linear and nonlinear components based on the light intensity and is expressed as $n_t(I) = n + n_2(I)$. The linear component 'n' is independent of light intensity, but the nonlinear component 'n_2' depends on light intensity. The relationship between the 'n' value and E_g of the film is given by the Dimitrov and Sakka relation:[58]

$$\frac{n^2 - 1}{n^2 + 2} = 1 - \sqrt{\frac{E_g}{20}} \quad (9)$$

The obtained values, as presented in Table 3, indicate a decrease with an increase in the laser irradiation time. It is found that 'n' decreased from 2.935 (unirradiated) to 2.832 upon a 60-min irradiation. This reduction in 'n' value is related to the increase in 'E_g' by Moss rule ($E_g n^4$ = constant).[59] The refractive index values are close to and in the range of 2 to 3 for the undoped and In^{3+} doped $Cu_{12}Sb_4S_{13}$ thin films.[60] The change in crystallinity is the cause for such changes in both parameters. There are various other models that establish the relationship between the bandgap and the refractive index. Further modification of the Moss formula with the constant value taken as 108 eV is expressed as,[61–63]

$$n_M = \sqrt[4]{\frac{108}{E_g}} \quad (9a)$$

This relation, on further simplification by considering the difference between the average and the optical energy gap, is written as[64]

$$n_R = 4.084 - [0.62 \times E_g] \quad (9b)$$

However, this relation is valid for the semiconducting material with a bandgap of less than ~4 eV. For the present study, this relation holds well as the bandgaps of all the films lie below 4 eV, as presented in Table 3. Herve–Vandamme formulated another relation for the low bandgap materials with the help of

Table 3 Optical parameters for the laser-irradiated films

Sample	E_g (eV)	B^2 ($\times 10^{10}$)	E_u (meV)	n_o	ε_L	$\chi^{(1)}$	$\chi^{(3)}$ ($\times 10^{-11}$ esu)	n_2 ($\times 10^{-10}$ esu)	η_{opt}	($\sigma \times 10^{-2}$)	S_{e-p}
0 min	1.59	6.22	411	2.93	8.61	0.60	2.30	2.95	1.71	6.28	10.61
5 min	1.62	6.42	385	2.92	8.52	0.59	2.19	2.83	1.71	6.71	9.92
10 min	1.65	7.13	374	2.90	8.42	0.59	2.08	2.70	1.72	6.91	9.64
30 min	1.69	8.55	365	2.88	8.31	0.58	1.95	2.55	1.72	7.08	9.41
60 min	1.79	9.13	353	2.83	8.02	0.55	1.66	2.20	1.73	7.32	9.11

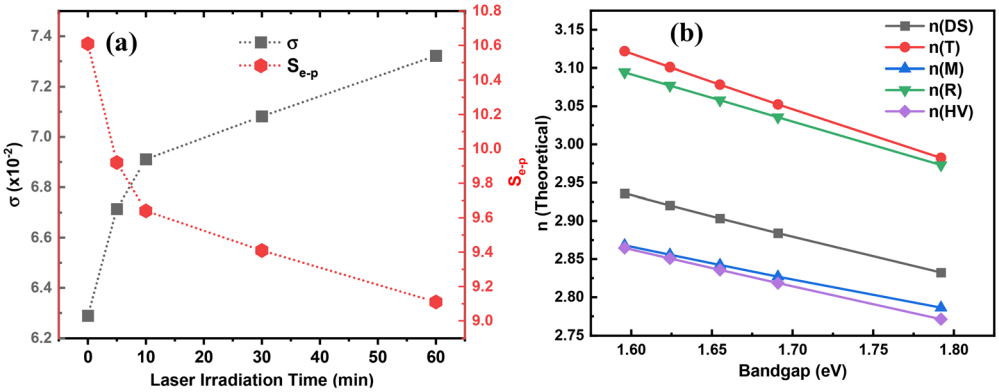

Fig. 9 (a) Variation in σ and S_{e-p}. (b) Theoretical refractive index from various models for the films.

oscillator theory, as[65]

$$n^2 = 1 + \left(\frac{A}{E_g + B}\right)^2 \quad (9c)$$

with $A \cong 13.6$ eV, (~hydrogen ionization energy), and B = 3.4 eV is the difference in energy between the UV resonance energy and E_g. The relation is rewritten as follows: considering these values, the above relation becomes

$$n_{[HV]} = \sqrt{1 + \left(\frac{13.6}{E_g + 3.47}\right)^2} \quad (9d)$$

Tripathy relation shows the exponential decay of 'n' for semiconductors as[66]

$$n_T = 1.73 \times [1 + 1.9017 \times e^{-0.539 \times E_g}] \quad (9e)$$

This relation is valid for a wide frequency range and also fits with the experimental results proposed by various authors. Fig. 9(b) shows the refractive index of all the films by various models, as discussed above. The lattice dielectric constant (ε_L) is determined through $\varepsilon_L = n^2$ (Table 3). The ε_L value is found to be decreasing from 8.619 to 8.022 upon laser irradiation. The high-frequency dielectric constant is associated with a free charge carrier that influences the polarization in the material. The values of optical conductivity (η_{opt}) are estimated from the equation,

$$\eta_{opt} = \left(\frac{C}{n_0}\right)^{1/4} \quad (9f)$$

The η_{opt} values are tabulated in Table 3. It is found that the η_{opt} values increased gradually with laser irradiation; however, the change is very small.

3.5. Nonlinear optical study

The high intensity of electromagnetic radiation incident on the material surface changes the bond size, nuclear interaction, electronic polarization, and other associated quantities.[67] The observed changes by such processes are helpful in many areas, like soliton propagation in optical telecommunications fibers, modulators, signal processing devices, switching circuits, *etc.*[68,69] The polarization density (P) in such cases is expressed as,

$$P = \varepsilon_0 \chi E = \varepsilon_0[\chi^{(1)}E + \chi^{(2)}E^2 + \chi^{(3)}E^3 \ldots \quad (10a)$$

Here, χ is the net susceptibility, and ε_0 represents the electrical permittivity of free space. E is the electric field intensity. The nonlinear susceptibility, $\chi = \chi^{(L)} + \chi^{(NL)}$ holds the linear part as $\chi^{(L)} = \chi^{(1)}$ and the nonlinear part as $\chi^{(NL)} = \chi^{(2)} + \chi^{(3)}$. Here χ^1, χ^2, and χ^3 are 1st, 2nd, and 3rd-order susceptibilities. However, the contribution from χ^2 is zero due to the centro-symmetric nature of chalcogenides. The relationships connecting $\chi^{(1)}$ and $\chi^{(3)}$ are,[70]

$$\chi^{(1)} = \frac{(n^2 - 1)}{4\pi} \quad \text{and} \quad \chi^{(3)} = A\frac{(n^2 - 1)^4}{(4\pi)^4} \quad (10b)$$

with $A = 1.7 \times 10^{-10}$ esu, the $(\chi^{(1)})$ and $(\chi^{(3)})$ values decreased with laser irradiation, as found in Table 3. It is found that both $\chi^{(1)}$ and $(\chi^{(3)})$ values vary inversely with E_g. Generally, it is considered that the χ value decreases with an increase in E_g and a decrease in the density of states. Such a change is observed for the studied thin films. The cause of such a laser-irradiated susceptibility change is homogenization and polymerization due to crystallization. Fig. 10(a) infers the change in both n_2 and $\chi^{(3)}$ at different laser illumination conditions.

According to Ticha's and Tichy's relation,[70] n_2 is related to $\chi^{(3)}$ and static refractive index (n_0) by the equation,

$$n_2 = \frac{12\pi\chi^{(3)}}{n_0} \quad (10c)$$

The n_2 value decreased with irradiation for the $Cu_{40}Sb_{40}S_{20}$ thin films from 2.302×10^{-11} esu to 1.661×10^{-11} esu for 60 m irradiation. The obtained values of n_2 for various films are given in Table 3. The enhanced structural ordering in irradiated films causes a reduction in the density of defects, which later accounts for the reduced value of nonlinearity by annealing, and thus, it is suitable for solid-state lasers and UV nonlinear materials.[71]

The photoluminescence (PL) spectra were taken for all $Cu_{40}Sb_{40}S_{20}$ films within the wavelength range of ~550–850 nm using 532 nm laser excitation. PL signifies the recombination of the hole–electron pairs, leading to photon

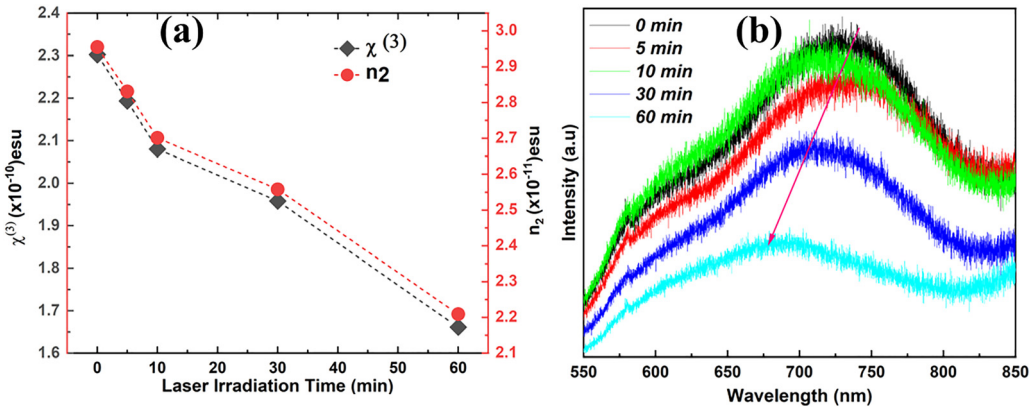

Fig. 10 (a) Change in $\chi^{(3)}$ and n_2 at different laser irradiation times. (b) PL spectra of all the films.

emission. The PL spectra of all the films are presented in Fig. 10(b). It was found that the peak appeared at 730 nm for the unirradiated film with high intensity. However, the intensity decreased with laser irradiation, as evident from Fig. 10(b). The decreased PL intensity signifies the decreased defect states. The peak position shifted towards a lower wavelength, inferring an increase in the bandgap. The PL peak for the 60-minute laser-irradiated film is ~677 nm. Such a shift in the PL spectra is due to the laser-induced changes by improved carrier mobility that change the electron–hole recombination dynamics.[72,73]

3.6. Photo response study by *I–V* measurements

The $Cu_{40}Sb_{40}S_{20}$ films were scraped on both sides to leave an undamaged film portion of 5 mm × 5 mm on the glass substrate for *IV* measurement. For conductive connections, Ag paste was applied on the two opposing faces of the film. The two created probes from the sample surface were then attached to a Keithley 2450 Source meter. A 9 W white LED bulb was used for the photodetection measurement, which was carried out in ambient settings. To minimize the possible effects of excessive local heating, white light sources were used to cover the whole visible spectrum. The *I–V* characteristic curves of all the irradiated and un-irradiated films under both dark and light conditions are illustrated in Fig. 11(a and b). Fig. S4 shows the individual *I–V* plots for each sample, which clearly show a larger current value under light conditions than dark conditions due to the absorption of more photons.[74,75] This enhancement in photocurrent is ascribed to light–material interactions along with charge separation. From the data in Fig. S4, the maximum current values under illuminated (I_L) and dark (I_D) conditions were extracted and are summarized in Table 4. The photosensitivity of the thin films was calculated using the equation mentioned below.[76,77] The key performance metrics for photodetectors, such as photoresponsivity (R) and detectivity (D^*), which are essential for assessing the photodetector efficiency, were calculated using specific mathematical relations and are also listed in Table 4.

$$\text{Photo sensitivity} = \frac{I_L - I_D}{I_D} \times 100\% \quad (11a)$$

$$\text{Responsivity}\,(R) = \frac{I_L}{A \times P_{in}} \quad (11b)$$

$$\text{Detectivity}\,(D*) = R\sqrt{\frac{A}{2eI_D}} \quad (11c)$$

Here, A represents the photodetector active surface area, *i.e.*, 0.25 cm^2. P_{in} is the power density of the incident light, which is ~20 mW cm^{-2}.

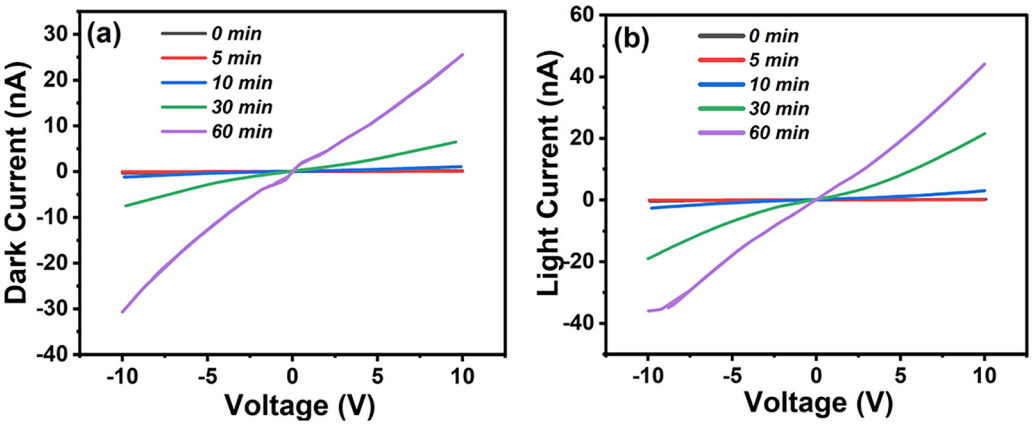

Fig. 11 *I–V* characteristic plots of all the $Cu_{40}Sb_{40}S_{20}$ films under (a) dark and (b) light conditions.

Table 4 The figure of merit of the irradiated and unirradiated films

Sample	I_L (nA)	I_D (nA)	$I_L - I_D$ (nA)	Photo sensitivity (%)	Responsivity (R) (A W^{-1})	Detectivity (D^*) (Jones)
0 min	0.211	0.175	0.036	20.57	4.22×10^{-8}	2.81×10^{6}
5 min	0.08	0.069	0.011	15.94	1.6×10^{-8}	1.7×10^{6}
10 min	3.01	1.06	1.95	183.96	6.02×10^{-7}	1.63×10^{7}
30 min	21.56	6.34	15.22	240.06	4.31×10^{-6}	4.78×10^{7}
60 min	44.06	25.56	18.5	272.37	8.81×10^{-6}	4.81×10^{7}

The photo response properties of the $Cu_{40}Sb_{40}S_{20}$ film upon laser irradiation were analysed using *I–V* characteristics and performance metrics, such as photosensitivity, responsivity, and detectivity. The *I–V* plots reveal that dark current remains relatively low and stable across all irradiation times. On the other hand, the photo current increased significantly with prolonged irradiation, and was found to be higher for the 60-minute irradiated film. This indicates the improved photo-generated carrier transport. Table 4 shows that photosensitivity increased consistently from 20.57% (0 min) to 272% (60 min). It shows a drastic increment in photo response. Responsivity, although fluctuating slightly, reached around 8.81×10^{-6} A W^{-1} for the 60-minute laser-treated film from 1.6×10^{-8} A W^{-1} of the un-irradiated film. Similarly, the detectivity improved from 1.7×10^{6} Jones initially to 4.81×10^{7} Jones after 60 minutes of laser irradiation. This indicates enhanced signal-to-noise performance.

The increasing laser irradiation time period plays an important role in shaping the photoresponse properties of $Cu_{40}Sb_{40}S_{20}$ films, in particular on the bandgap of the material. As the laser irradiation time is enhanced, it typically induces structural reorganization, which often leads to an increase in the optical bandgap of the films. A widening bandgap generally enhances the selectivity of the material to incident photons of specific energies, suppressing thermally activated carriers that contribute to dark current. This explains the observed reduction in dark current (I_D) with prolonged irradiation, as seen in Fig. 11(a). The low value of dark current expands the signal-to-noise ratio, a key factor reflected in the increased detectivity (D^*) values.

At the same time, a larger bandgap can reduce the number of absorbed photons, enhance the efficiency of carrier separation, and reduce recombination of the film's internal order. Thus, the increase in bandgap acts as a double-edged factor: it narrows the light absorption window slightly but sharpens the film's ability to distinguish between light and dark conditions, leading to more reliable photodetection behavior.

In summary, the higher bandgap values at higher irradiation times tune the balance between photon absorption and carrier concentration. It reduces the dark currents and improves the photosensitivity and detectivity of laser-irradiated films. It creates fewer traps and better carrier mobility, which is essential for high-performance photodetectors.[78] The observed results suggest that laser annealing, particularly at longer durations (60 minutes), significantly enhances the optoelectronic quality of $Cu_{40}Sb_{40}S_{20}$ films by improving carrier separation and defect management. Consequently, the films exhibit stronger photodetector characteristics with higher photosensitivity and detectivity, making them more suitable for sensitive photodetection applications in the UV-visible region.

4. Conclusion

The time-dependent laser irradiation results from the $Cu_{40}Sb_{40}S_{20}$ film show a significant improvement in photodetectivity, 4.81×10^{7} Jones, and responsivity by three-fold, compared to the un-irradiated film. The thermally evaporated $Cu_{40}Sb_{40}S_{20}$ films were subjected to laser irradiation at different time scales, inferring the change in crystallinity as observed from the XRD analysis. The average crystallite size decreased from 21.66 nm to 16.49 nm, along with an increase in dislocation density from 2.131×10^{-3} to 3.677×10^{-3} nm^{-2} and lattice strain. The surface of the films gets modified with higher porosity with laser illumination. The hydrophobicity quality remained unchanged, with a slight decrease in the contact angle value, even after laser irradiation, which is very useful for self-cleaning. The Raman spectra intensity change revealed microstructural modification with laser treatment. The shift in the PL peak with decreased intensity implies a decrease in defect states, thus increasing the bandgap. The increase in transmittance from 55% to 97% upon laser illumination brings down the absorption capability, making the film more transparent. The extinction coefficient and optical density decreased with the increase in the laser annealing time. The optical bandgap increased from 1.596 to 1.792 eV upon 60-minute irradiation. The Urbach energy decreased, implying the structural order. The static refractive index thus decreased with a reduction in optical nonlinearity in terms of the 3rd-order susceptibility from 2.302×10^{-11} esu to 1.661×10^{-11} esu after 60-minute laser treatment. The corresponding nonlinear refractive index decreased from 2.955×10^{-10} esu to 2.209×10^{-10} esu. However, the optical conductivity increased from 1.717 to 1.732 upon 60-minute irradiation. The obtained changes in the films with laser treatment are useful for optoelectronic applications. The noticed changes in the photo response parameters are very useful for photo detection in the visible range.

Conflicts of interest

The authors declare no conflicts of interest.

Data availability

The data supporting this article have been included as part of the SI. Supplementary information: EDX spectra, elemental

mapping, individual bandgap calculation, and *IV* plots of the thin films. See DOI: https://doi.org/10.1039/d5ma00505a.

Acknowledgements

Dr R. Naik acknowledges the ICT-IOC instrumentation facility and the Science and Engineering Research Board, Govt. of India.

References

1 Z. Aftab, I. Sulania, A. Kandasami and L. Nair, Swift heavy ion-induced reactivity and surface modifications in indium thin films, *ACS Omega*, 2022, **7**, 31869–31876.
2 P. Priyadarshini, D. Alagarasan, R. Ganesan, S. Varadharajaperumal and R. Naik, Influence of proton ion irradiation on the linear–nonlinear optoelectronic properties of $Sb_{40}Se_{20}S_{40}$ thin films at different fluences for photonic devices, *ACS Appl. Opt. Mater.*, 2023, **1**, 55–68.
3 F. Chandoul, A. Boukhachem, F. Hosni, H. Moussa, M. S. Fayache and M. Amlouk, Change of the properties of nanostructured MoO_3 thin films using gamma-ray irradiation, *Ceram. Int.*, 2018, **44**, 12483–12490.
4 S. Das, S. Senapati, D. Alagarasan, S. Varadhrajaperumal, R. Ganesan and R. Naik, Thermal annealing-induced transformation of structural, morphological, linear, and nonlinear optical parameters of quaternary $As_{20}Ag_{10}Te_{10}Se_{60}$ thin films for optical applications, *ACS Appl. Opt. Mater.*, 2023, **1**, 17–31.
5 P. Pradhan, R. Naik, N. Das and A. K. Panda, Band gap tuning in $As_{40}Se_{53}Sb_{07}$ thin films by 532 nm laser irradiation: An optical investigation by spectroscopic techniques, *Opt. Mater.*, 2018, **75**, 699–709.
6 H. Palneedi, J. H. Park, D. Maurya, M. Peddigari, G. T. Hwang, V. Annapureddy, J. W. Kim, J. J. Choi, B. D. Hahn, S. Priya, K. J. Lee and J. Ryu, Laser irradiation of metal oxide films and nanostructures: applications and advances, *Adv. Mater.*, 2018, **30**, 1705148.
7 O. V. Overschelde, G. Guisbiers and M. Wantelet, Nanocrystallization of Anatase or Rutile TiO_2 by Laser Treatment, *J. Phys. Chem. C*, 2009, **113**, 15343–15345.
8 H. Lu, Y. Tu, X. Lin, B. Fang, D. Luo and A. Laaksonen, Effects of laser irradiation on the structure and optical properties of ZnO thin films, *Mater. Lett.*, 2010, **64**, 2072–2075.
9 M. I. Khan and Asghar Ali, Effect of laser irradiation on the structural, morphological and electrical properties of polycrystalline TiO_2 thin films, *Res. Phys.*, 2017, **7**, 3455–3458.
10 K. C. Phillips, H. H. Gandhi, E. Mazur and S. K. Sundaram, Ultrafast laser processing of materials: a review, *Adv. Opt. Photonics*, 2015, **7**, 684–712.
11 Y. Hou and A. H. Jayatissa, Effect of laser irradiation on gas sensing properties of sol-gel derived nanocrystalline Al-doped ZnO thin films, *Thin Solid Films*, 2014, **562**, 585–591.
12 K. Tanaka, Photo-induced phenomena in chalcogenide glass: Comparison with those in oxide glass and polymer, *J. Non-Cryst. Solids*, 2006, **352**, 2580–2584.
13 J. S. Brian, J. M. Helen, M. Sudhajit, F. Christos, J. D. Phillip and A. S. Michael, Laser processing for thin film chalcogenide photovoltaics: a review and prospectus, *J. Photon. Energy*, 2015, **5**, 1–20.
14 A. A. Al-Ghamdi, S. A. Khan, S. Al-Heniti, F. A. Al-Agel, T. Al-Harbi and M. Zulfequar, Effects of laser irradiation on optical properties of amorphous and annealed $Ga_{15}Se_{81}In_4$ and $Ga_{15}Se_{79}In_6$ chalcogenide thin films, *J. Alloys Compd.*, 2010, **505**, 229–234.
15 R. Naik, S. Jena, R. Ganesan and N. K. Sahoo, Laser-induced optical properties change in $Sb_{10}S_{40}Se_{50}$ chalcogenide thin films: An investigation through FTIR and XPS measurements, *Phys. Status Solid B*, 2014, **251**, 661–664.
16 S. A. Khan and A. A. Al-Ghamdi, Influence of laser-irradiation on the optical constants $Se_{75}S_{25-x}Cd_x$ thin films, *Mater. Lett.*, 2009, **63**, 1740–1742.
17 M. A. Alvi, M. Zulfequar and A. A. Al-Ghamdi, Characterization of phase change $Ga_{15}Se_{77}Ag_8$ chalcogenide thin films by laser-irradiation, *J. Alloys Compd.*, 2013, **550**, 431–437.
18 G. Mao, F. Chen, W. Wang, Z. Li, C. Jia and Y. Liu, Effect of femtosecond laser irradiation on photostability of chalcogenide thin films within a Ge-S binary system, *Opt. Laser Technol.*, 2023, **166**, 109641.
19 S. Ahmad, K. Asokan and M. Zulfequar, Laser irradiation induced photo-crystallization in nano-structured amorphous $Se_{90-x}Hg_xS_{10}$ (x = 0, 5, 10, 15) thin films, *RSC Adv.*, 2016, **6**, 44321–44332.
20 K. T. Paula, N. S. Dutta, J. M. P. Almeida, L. K. Nolasco, M. B. Andrade, C. B. Arnold and C. R. Mendonça, Femtosecond laser-induced damage threshold incubation and oxidation in AS_2S_3 and AS_2Se_3 thin films, *Appl. Surf. Sci.*, 2024, **654**, 159449.
21 P. Kutálek, P. Knotek, A. Šandová, T. Vaculovič, E. Černošková and L. Tichý, Ablation of binary As_2S_3, As_2Se_3, GeS_2, $GeSe_2$ and $GeSe_3$ bulk glasses and thin films with a deep ultraviolet nanosecond laser, *Appl. Surf. Sci.*, 2021, **554**, 149582.
22 A. Collado-Hernandeza, M. García-Mendeza, M. I. Mendívil-Palmab, C. Gomez-Rodríguezc, D. Fernandez-Gonzalezd and L. V. García-Quinonez, Effect of laser irradiation on RF-sputtered antimony sulfide thin films, *Vacuum*, 2023, **211**, 111925.
23 P. Khan and K. V. Adarsh, Light-induced effects in amorphous chalcogenide glasses: femtoseconds to seconds, *Physics*, 2021, **3**, 255–274.
24 A. Parida, D. Alagarasan, R. Ganesan, S. Bisoyi and R. Naik, Influence of time-dependent laser-irradiation for tuning the linear–nonlinear optical response of quaternary $Ag_{10}In_{15}S_{15}Se_{60}$ films for optoelectronic applications, *RSC Adv.*, 2023, **13**, 4236.
25 A. Parida, D. Alagarasan, G. K. Pradhan and R. Naik, Time-dependent 532 nm laser irradiation on quaternary $Sb_{10}S_{15}In_{15}Se_{60}$ films: An insight into its structural, morphological, and optical modifications for photonics application, *Phys. B: Cond. Matter*, 2023, **657**, 414785.
26 P. Priyadarshini, A. Parida, D. Alagarasan, R. Ganesan and R. Naik, Time-dependent laser irradiation-induced kinetics

of changes in linear–nonlinear optical properties of $Bi_{15}In_{20}Se_{65}$ thin films for IR applications, *J. Appl. Phys.*, 2023, **133**, 063104.

27 S. Das, A. Parida, D. Alagarasan and R. Naik, Time-dependent laser irradiation induced structural, linear-nonlinear optical changes in $Ag_{10}Te_{10}As_{20}Se_{60}$ quaternary film for optoelectronic applications, *Eur. Phys. J. Plus*, 2022, **138**, 639.

28 B. J. Jena, S. Das, S. Senapati and R. Naik, Stability of Ag_2S/As_2Se_3 thin films under time-dependent laser irradiation and its impact on linear-nonlinear optical properties for optoelectronic applications, *Opt. Laser Technol.*, 2023, **164**, 109461.

29 A. Ganjoo, K. Shimakawa, H. Kamiya, E. A. Davis and J. Singh, *Phys. Rev. B: Condens. Matter Mater. Phys.*, 2000, **62**, R14601.

30 R. Naik, C. Sripan and R. Ganesan, Photo darkening in $As_{50}Se_{50}$ thin films by 532 nm laser irradiation, *Opt. Laser Technol.*, 2017, **90**, 158–164.

31 C. R. Crick and I. P. Parkin, Preparation and characterization of super-hydrophobic surfaces, *Chem. – Eur. J.*, 2010, **16**, 3568–3588.

32 S. Giri, P. Priyadarshini, D. Alagarasan, R. Ganesan and R. Naik, Influence of Te replacement by Bi in $In_{10}Se_{70}Te_{20-x}Bi_x$ films and its structural, optical, morphological, surface wettability and thermal behaviors for optoelectronic applications, *Opt. Mater.*, 2023, **146**, 114522.

33 B. Mohanty, S. Das, P. C. Kumar, D. Alagarasan, R. Ganesan and R. Naik, Exploring the optical, structural, and surface wettability of thermally evaporated $Ag_{25}S_{35}Se_{40}$ thin films by annealing for optoelectronic applications, *Phys. B: Cond. Matter*, 2025, **699**, 416823.

34 O. U. Nimittrakoolchai and S. Supothina, Deposition of organic-based superhydrophobic films for anti-adhesion and self-cleaning applications, *J. Eur. Ceram. Soc.*, 2008, **28**, 947–952.

35 T. Halenkovic, M. Baillieul, J. Gutwirth, P. Nemec and V. Nazabal, Amorphous Ge-Sb- Se-Te chalcogenide films fabrication for potential environmental sensing and nonlinear photonics, *J. Mater.*, 2022, **8**, 1009–1019.

36 U. Chalapathi, P. U. Bhaskar, S. Sangaraju, B. A. Al-Asbahi and S. H. Park, $CuSbS_2$ thin films and solar cells produced from Cu/Sb/Cu stacks via sulfurization, *Heliyon*, 2024, **10**, e27504.

37 E. J. Mittemeijer and U. Welzel, The ''state of the art'' of the diffraction analysis of crystallite size and lattice strain, *Z. Kristallogr.*, 2008, **223**, 552–560.

38 K. He, N. Chen, C. Wang, L. Wei and J. Chen, Method for determining crystal grain size by x-ray diffraction, *Cryst. Res. Technol.*, 2018, **53**, 1700157.

39 S. Das, S. Senapati, J. Kumar and R. Naik, Photo-induced interfacial mixing of Sb/Ag_2Se heterojunction layers at a different lasing time for tuning its linear-nonlinear optical properties for optoelectronic applications: An experimental and computational study, *Surf. Interfaces*, 2024, **48**, 104298.

40 A. Parida, S. Senapati and G. K. Pradhan, Tailoring optical properties of hydrothermally synthesized SnMnSe nanocubes for optoelectronic and dielectric applications, *J. Alloys Compd.*, 2024, **970**, 172520.

41 D. S. P. Kumar, M. Ren, T. Osipowicz, R. C. Mallik and P. Malar, Tetrahedrite ($Cu_{12}Sb_4S_{13}$) thin films for photovoltaic and thermoelectric applications, *Sol. Energy*, 2018, **174**, 422–430.

42 T. Alqahtani, M. D. Khan, D. J. Lewis, X. L. Zhong and P. O'Brien, Scalable synthesis of Cu–Sb–S phases from reactive melts of metal xanthates and effect of cationic manipulation on structural and optical properties, *Sci. Rep.*, 2021, **11**, 1887.

43 S. V. Vinayakumar, S. Shaji, D. Avellaneda, T. K. Das Roy, G. A. Castillo, J. A. A. Martinez and B. Krishnan, $CuSbS_2$ thin films by rapid thermal processing of Sb_2S_3-Cu stack layers for photovoltaic application, *Solar Energy Mater. Solar Cells*, 2017, **164**, 19–27.

44 T. Rath, A. J. MacLachlan, M. D. Brown and S. A. Haque, Structural, optical and charge generation properties of chalcostibite and tetrahedrite copper antimony sulfide thin films prepared from metal xanthates, *J. Mater. Chem. A*, 2015, **3**, 24155–24162.

45 V. P. Zakaznova-Herzog, S. L. Harmer, H. W. Nesbitt, G. M. Bancroft, R. Flemming and A. R. Pratt, High resolution XPS study of the large-band-gap semiconductor stibnite (Sb_2S_3): Structural contributions and surface reconstruction, *Surf. Sci.*, 2006, **600**, 348–356.

46 S. Das, S. Senapati, D. Alagarasan and R. Naik, Laser-induced modification in structural, morphological, linear and nonlinear optical parameters of $Ge_{20}Ag_{10}Te_{10}Se_{60}$ thin films for optoelectronic applications, *Mater. Sci. Semicond. Process.*, 2023, **160**, 107456.

47 J. Tauc, *Amorphous and Liquid Semiconductors*, Plenum Press, New York, 1979, p. 159.

48 M. Behera and R. Naik, Optical properties change in laser-induced Te/As_2Se_3 chalcogenide thin films, *Appl. Phys. A: Mater. Sci. Process.*, 2016, **122**, 913.

49 P. Priyadarshini, S. Das, D. Alagarasan, R. Ganesan, S. Vardharajperumal and R. Naik, Observation of high nonlinearity in Bi doped $Bi_xIn_{35-x}Se_{65}$ thin films with annealing, *Sci. Rep.*, 2021, **11**, 21518.

50 P. Chaiworn, A. Kambut, P. Pluengphon, E. Wongrat, C. Wichasilp and A. Tubtimtae, Aluminum antimony alloy overlayers synthesized using the electrodeposition method: investigation of structural, optical, electrical properties, and DFT calculation, *Semicond. Sci. Technol.*, 2024, **39**, 115012.

51 G. Abbady, A. Qasem and A. M. Abd-Elnaiem, Optical parameters and electronic properties for the transition of the amorphous-crystalline phase in $Ge_{20}Te_{80}$ thin films, *J. Alloys Compd.*, 2020, **842**, 155705.

52 F. Urbach, The long-wavelength edge of photographic sensitivity and of the electronic absorption of solids, *Phys. Rev.*, 1953, **92**, 1324.

53 S. Das, P. Priyadarshini, D. Alagarasan, S. Varadharajaperumal, R. Ganesan and R. Naik, Role of tellurium addition on the linear and nonlinear optical, structural, morphological properties of $Ag_{60-x}Se_{40}Te_x$ thin films for nonlinear applications, *J. Am. Ceram. Soc.*, 2022, **105**, 3469–3484.

54 N. Chaudhary, S. K. Tripathi and N. Goya, Deviation in tuning of optical properties of polycrystalline Ag-Se-Te thin films, *Integr. Ferroelectr.*, 2018, **186**, 84–90.
55 A. M. Abd-Elnaiem, S. Moustafa, A. Abdelraheeem, M. A. Abdel-Rahim and A. Z. Mahmoud, Effects of annealing on structural and optical properties of $Ge_{20}Se_{70}Sn_{10}$ thin films for optoelectronic applications, *J. Non-Cryst. Solids*, 2020, **549**, 120353.
56 A. S. Hassanien and A. A. Akl, Effect of Se addition on optical and electrical properties of chalcogenide CdSSe thin films, *Superlattices Microstruct.*, 2016, **89**, 153–169.
57 S. Giri, P. Priyadarshini, D. Alagarasan, R. Ganesan and R. Naik, Annealing-induced phase transformation in $In_{10}Se_{70}Te_{20}$ thin films and its structural, optical and morphological changes for optoelectronic applications, *RSC Adv.*, 2023, **13**, 24955–24972.
58 V. Dimitrov and S. Sakka, Linear and nonlinear optical properties of simple oxides, *J. Appl. Phys.*, 1996, **79**, 1741.
59 T. S. Moss, A relationship between the refractive index and the infra-red threshold of sensitivity for photoconductors, *Proc. Phys. Soc. Sec.*, 1950, **63**, 167–176.
60 P. Suttiyarak and A. Tubtimtae, P-type In^{3+}-doped $Cu_{12}Sb_4S_{13}$ thin films deposited by spray pyrolysis method: Investigation of structural, optical, electrical, and electrocatalytic properties, *Appl. Surf. Sci.*, 2020, **527**, 146835.
61 A. Lamichhane, Energy-gap-refractive index relations in semiconductors—Using wemple–DiDomenico model to unify moss, ravindra, and herve–vandamme relationships, *Solids*, 2023, **4**, 316–326.
62 V. P. Gupta and N. M. Ravindra, Comments on the moss formula, *Phys. Status Solidi B*, 1980, **100**, 715–719.
63 N. M. Ravindra, P. Ganapathy and J. Choi, Energy gap–refractive index relations in semiconductors–An overview, *Infrared Phys. Tech.*, 2007, **50**, 21–29.
64 N. M. Ravindra, S. Auluck and V. K. Srivastava, On the penn gap in semiconductors, *Phys. Status Solidi B*, 1979, **93**, 155–160.
65 P. Herve and L. K. J. Vandamme, General relation between refractive index and energy gap in semiconductors, *Infrared Phys. Technol.*, 1994, **35**, 609–615.
66 S. K. Tripathy, Refractive indices of semiconductors from energy gaps, *Opt. Mater.*, 2015, **46**, 240–246.
67 V. Sasikala and K. Chitra, All-optical switching and associated technologies: A review, *J. Opt.*, 2018, **47**, 307–317.
68 G. Li, S. Chen, N. Pholchai, B. Reineke, P. W. H. Wong, E. Y. B. Pun, K. W. Cheah, T. Zentgraf and S. Zhang, Continuous control of the nonlinearity phase for harmonic generations, *Nat. Mater.*, 2015, **14**, 607–612.
69 D. Sahoo, S. Sahoo, D. Alagarasan, R. Ganesan, S. Varadharajaperumal and R. Naik, Proton ion irradiation on $As_{40}Se_{50}Sb_{10}$ thin films: fluence-dependent tuning of linear–nonlinear optical properties for photonic applications, *ACS Appl. Elect. Mater.*, 2022, **4**, 856–868.
70 H. Ticha and L. Tichy, Semiempirical relation between nonlinear susceptibility (refractive index), linear refractive index and optical gap and its application to amorphous chalcogenides, *J. Optoelectron. Adv. Mater.*, 2002, **4**, 381–386.
71 X. Dong, L. Huang, Q. Liu, H. Zeng, Z. Lin, D. Xu and G. Zou, Perfect balance harmony in $Ba_2NO_3(OH)_3$: a beryllium-free nitrate as a UV nonlinear optical material, *Chem. Commun.*, 2018, **54**, 5792–5795.
72 B. K. Gupta, R. Sultana, S. Singh, V. Singh, G. Awana, A. Gupta, B. Singh, A. K. Srivastava, O. N. Srivastava, S. Auluck and V. P. S. Awana, Unexplored photoluminescence from bulk and mechanically exfoliated few layers of Bi_2Te_3, *Sci. Rep.*, 2018, **8**, 9205.
73 S. Das, S. Senapati, D. Alagarasan and R. Naik, Temperature-dependent Raman and Photo response studies of Bi_2Te_3 thin films annealed at different temperatures for improved optoelectronic performance, *Mater. Adv.*, 2024, **5**, 3379.
74 D. Alagarasan, S. Varadharajaperumal, K. D. A. Kumar, R. Naik and A. Arunkumar, Optimization of different temperature annealed nanostructured CdSe thin film for photodetector applications, *Opt. Mater.*, 2021, **122**, 111706.
75 P. Priyadarshini, P. C. Kumar and R. Naik, Tuning in optoelectronic properties of In/Te bilayer heterostructure upon annealing at different temperatures: surface wettability and photo response study for photonic and solar cell applications, *RSC Adv.*, 2024, **14**, 12897–12910.
76 D. Alagarasan, S. Vardharajaperumal, R. Naik and R. Ganesan, Effect of SnS thin film thickness on visible light photo detection, *Phys. Scr.*, 2022, **97**, 065814.
77 P. C. Kumar, S. Kanungo, P. Pradhan, S. K. Biswal, J. Kumar, C. Sripan and R. Naik, Tuning hydrophilicity and photoresponse by interfacial Ag diffusion in the Sb_2S_3 layer for optoelectronic applications: An experimental and computational study, *J. Phys. Chem. C*, 2024, **128**, 16740–16753.
78 W. Ouyang, F. Teng, J.-H. He and X. Fang, Enhancing the photoelectric performance of photodetectors based on metal oxide semiconductors by charge-carrier engineering, *Adv. Funct. Mater.*, 2019, **29**, 1807672.